Chapter 8
Dispersion of Impedances at Solid Electrodes

8.1 Constant Phase Element

The impedance of ideally polarizable liquid electrodes (e.g., mercury, amalgams, indium-gallium) may be modeled by an *R-C* circuit (Fig. 4.1a). However, most impedance studies are now carried out at solid electrodes. At these electrodes the double-layer capacitance is not purely capacitive and often displays a certain frequency dispersion. Such behavior cannot be modeled by a simple circuit consisting of R, L, and C elements. To explain such behavior, a constant phase element (CPE) is usually used.

In general, bulk dielectric dispersion in solids and liquids is well known and described in the literature [24, 297, 298]. In this chapter, the dispersion of capacitances at electrode surfaces in solutions will be discussed. The complex dielectric constant is described as

$$\frac{\varepsilon(\omega)-\varepsilon_\infty}{\varepsilon_S-\varepsilon_\infty}=\int_0^\infty \frac{G(\tau)}{1+j\omega\tau}\,d\tau, \tag{8.1}$$

where ε_∞ and ε_S are the dielectric constants at frequencies $\omega \to \infty$ and $\omega \to 0$ and $G(\tau)$ is the function describing the distribution of time constants. If there is no distribution of time constants, i.e., the dielectric constant may be described by one time constant, the function $G(\tau)$ is simply Dirac's δ function, $G(\tau) = \delta(\tau-\tau_0)$, and integration in Eq. (8.1) gives

$$\frac{\varepsilon(\omega)-\varepsilon_\infty}{\varepsilon_S-\varepsilon_\infty}=\frac{1}{1+j\omega\tau_0}. \tag{8.2}$$

A. Lasia, *Electrochemical Impedance Spectroscopy and its Applications*,
DOI 10.1007/978-1-4614-8933-7_8, © Springer Science+Business Media New York 2014

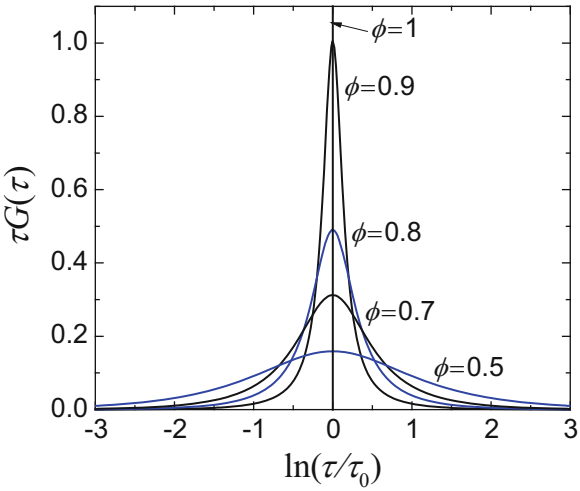

Fig. 8.1 Dependence of time constant distribution function, $\tau G(\tau)$, Eq. (8.5), on $\ln(\tau/\tau_0)$

Cole and Cole [297] described the observed dispersion by the function

$$\frac{\varepsilon(\omega)-\varepsilon_\infty}{\varepsilon_S-\varepsilon_\infty}=\frac{1}{1+(j\omega\tau_0)^\phi}, \tag{8.3}$$

where ϕ is the dimensionless parameter and $\phi \leq 1$. By analogy, the dispersion of impedances may be described by

$$\frac{\hat{Z}(\omega)-Z_\infty}{Z_0-Z_\infty}=\int_0^\infty \frac{\tau G(\tau)}{1+j\omega\tau}\mathrm{d}\ln\tau. \tag{8.4}$$

The distribution function is described by [297]

$$G(\tau)=\frac{1}{2\pi\tau}\frac{\sin[(1-\phi)\pi]}{\cosh[\phi\ln(\tau/\tau_0)]-\cos[(1-\phi)\pi]}, \tag{8.5}$$

and the plot of $\tau G(\tau)$ versus $\ln(\tau/\tau_0)$ is shown in Fig. 8.1. When $\phi = 1$, the distribution function reduces to Dirac's delta function, and with its decrease the distribution becomes wider around $\tau = \tau_0$.

In such a case, the impedance of the ideal capacitor, $1/(j\omega C)$, must be replaced by the impedance of a CPE:

$$\hat{Z}_{\mathrm{CPE}}=\frac{1}{T(j\omega)^\phi}, \tag{8.6}$$

where T is the parameter related to the electrode capacitance (F $s^{\phi-1}$ cm^{-2}), and ϕ is the constant phase exponent ($0 < \phi < 1$) related to the deviation of the straight

capacitive line from 90° by an angle $\alpha = 90°(1 - \phi)$. The units of T can also be rearranged [299] to Ω^{-1} s^{ϕ} cm^{-2}; however, as it becomes purely capacitive for $\phi = 1$, it seems more logical to use farads instead of ohms. Taking into account the properties of the complex numbers, $j^{\phi} = \cos(\phi\pi/2) - j\ \sin(\phi\pi/2)$ is a complex number and Eq. (8.6) may be expressed as

$$\hat{Z}_{\text{CPE}} = \left[\frac{\cos(\phi\pi/2)}{T\omega^{\phi}}\right] - j\left[\frac{\sin(\phi\pi/2)}{T\omega^{\phi}}\right], \tag{8.7}$$

which means that the impedance of this element is no longer purely imaginary and always contains both real and imaginary components. Therefore, the CPE represents a nonideal or "leaking capacitor" and causes energy dissipation because of the presence of the impedance real part [299–301]. In fact, the inverse transform of the CPE element into the time domain shows that after the potential step the current decreases proportionally to $t^{-\phi}$, that is, it never reaches zero [302], which means the electrode charge goes to infinity! Such an electrode cannot be called ideally polarizable [301] and it physically cannot exist. This means that somewhere beyond the measured low-frequency range it must become ideally polarizable. The name *constant phase element* originates from its behavior displayed on the complex plane and Bode plots in Fig. 8.2. The complex plane plots deviate from the ideal capacitor case by 9° for $\phi = 0.9$ and by 18° for $\phi = 0.8$. The Bode phase angle is always constant and equal to $90°\phi$, and the slope of the logarithmic Bode magnitude plots equals ϕ. In the absence of redox species in solution, the electrical equivalent circuit consists of a $R_s - CPE_{dl}$ connection in series. The corresponding complex plane and Bode plots are displayed in Fig. 8.3. The slopes in the complex plane plots are the same as in Fig. 8.2, and the Bode plots approach those for the CPE only at lower frequencies.

To more easily identify the presence of the CPE, Orazem et al. [303] proposed using Bode plots of impedances corrected for the solution resistance, $\log|Z''|$ versus $\log f$, and effective capacitance plots T_{eff} versus $\log f$:

$$T_{\text{eff}} = -\sin\left(\frac{\phi\pi}{2}\right)\frac{1}{Z''(2\pi f)^{\phi}}. \tag{8.8}$$

Such plots will be presented below (Fig. 8.5).

In the presence of a redox reaction without diffusion limitations, the system impedance is described by the electrical equivalent circuit $R_s(C_{dl}R_{ct})$ displayed in Fig. 2.34. Replacing the double-layer capacitance with the CPE produces complex plane and Bode plots (Fig. 8.4) corresponding to the equation for the impedance of such a system:

$$Z = R_s + \frac{1}{(j\omega)^{\phi}T + \frac{1}{R_{ct}}}. \tag{8.9}$$

The complex plane plots represent "sunken" or rotated semicircles with their center located below the real axis [304]. There are also changes in the Bode plots.

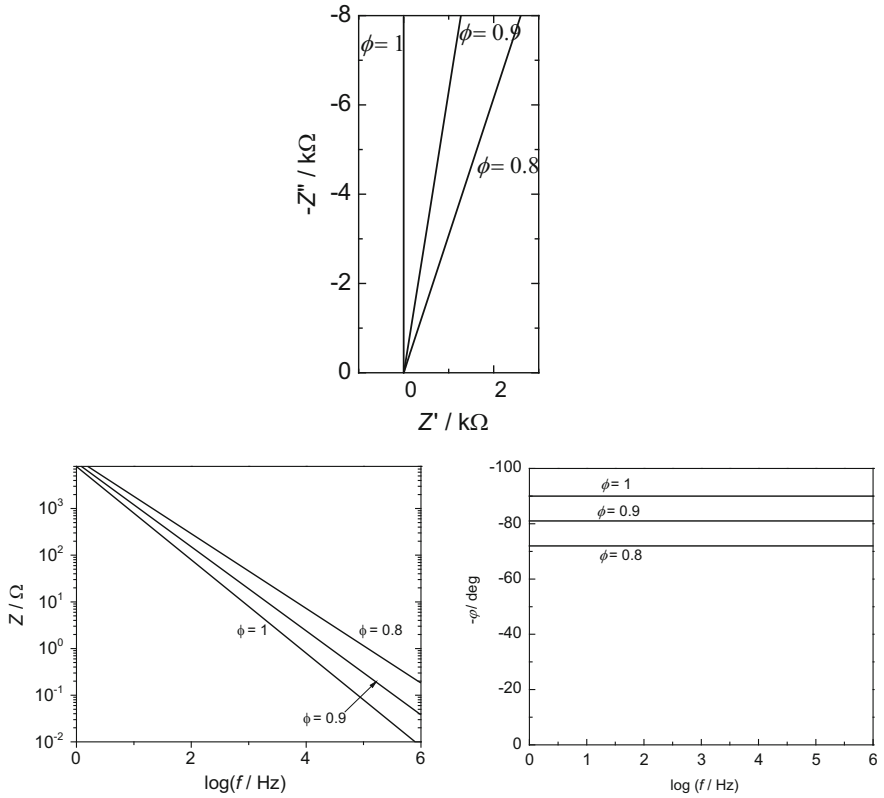

Fig. 8.2 Complex plane and Bode plots of CPE element, Eq. (8.6), for $T = 20\ \mu\text{F cm}^{-2}\ \text{s}^{\phi-1}$

The plots of $\log|Z''|$ versus $\log f$ and the effective capacitance plot of T_{eff} versus $\log f$ are displayed in Fig. 8.5. Note that such plots are very sensitive to variations in the CPE exponent, which is determined experimentally. Such a procedure could be used when the equivalent circuit describing the system is not known.

Brug et al. [305] proposed a simple model that allows estimation of an average double-layer capacitance, $\overline{C}_{\text{dl}}$, for the CPE behavior. The model consists of the solution resistance, R_{s}, and the CPE in series, R_{s}-*CPE*, i.e., electrode-supporting electrolyte interface. Assuming dispersion of the time constants, $\tau = R_{\text{s}}C_{\text{dl}}$, around an average value, $\tau_0 = R_{\text{s}}\overline{C}_{\text{dl}}$, and the Cole-Cole formula, Eq. (8.3), the researchers obtained

$$\hat{Z} = R_{\text{s}} + \frac{1}{(j\omega)^{\phi}T} = R_{\text{s}}\left[1 + \frac{1}{(j\omega)^{\phi}(R_{\text{s}}T)}\right] = R_{\text{s}}\left[1 + \frac{1}{(j\omega\tau_0)^{\phi}}\right]. \tag{8.10}$$

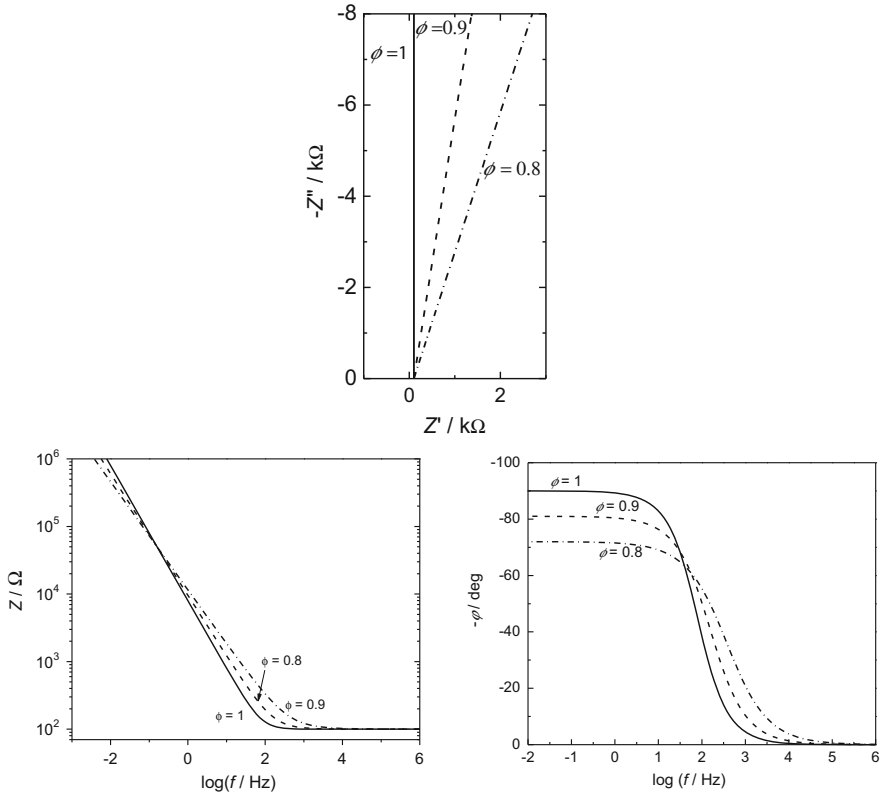

Fig. 8.3 Complex plane and Bode plots for the *R-CPE* circuit in series, $R = 100\ \Omega$, $T = 20\ \mu\text{F cm}^{-2}\ \text{s}^{\phi-1}$

Comparison of the terms in parentheses leads to

$$T = \overline{C}_{\text{dl}}^{\phi} R_{\text{s}}^{-(1-\phi)} \text{ or } C_{\text{dl}} = T^{1/\phi}\left(\frac{1}{R_{\text{s}}}\right)^{1-\frac{1}{\phi}}, \tag{8.11}$$

from which $\overline{C}_{\text{dl}}$ is obtained. In a similar way, for the circuit $R_{\text{s}}(CPE_{\text{dl}}R_{\text{ct}})$ (as in Fig. 2.34) they obtained

$$T = \overline{C}_{\text{dl}}{}^{\phi}\left[R_{\text{s}}^{-1} + R_{\text{ct}}^{-1}\right]^{1-\phi}. \tag{8.12}$$

Hsu and Mansfeld [306] proposed another formula that is applicable to cases where a semicircle is observed on complex plane plots:

$$\overline{C}_{\text{dl}} = T(\omega_{\text{c}})^{\phi-1}, \tag{8.13}$$

where ω_{c} is the frequency corresponding to the maximum of the imaginary part (corresponding to the maximum of the semicircle). This frequency may be calculated from [307]

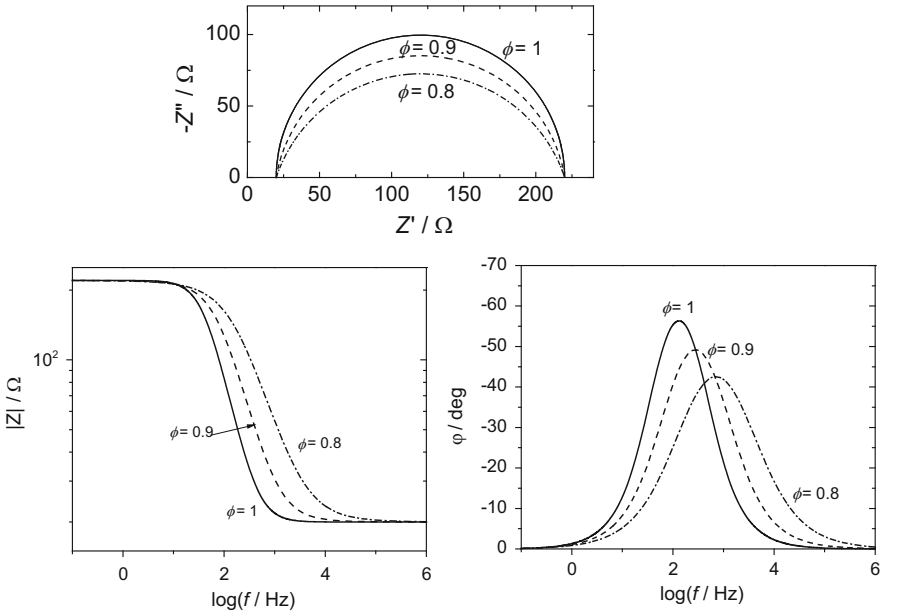

Fig. 8.4 Complex plane and Bode plots for circuit consisting of solution resistance in series with parallel connection of CPE and resistance R_{ct}. Parameters: $R_s = 10\ \Omega$, $T = 20\ \mu F\ cm^{-2}\ s^{\phi-1}$, $R_{ct} = 200\ \Omega$

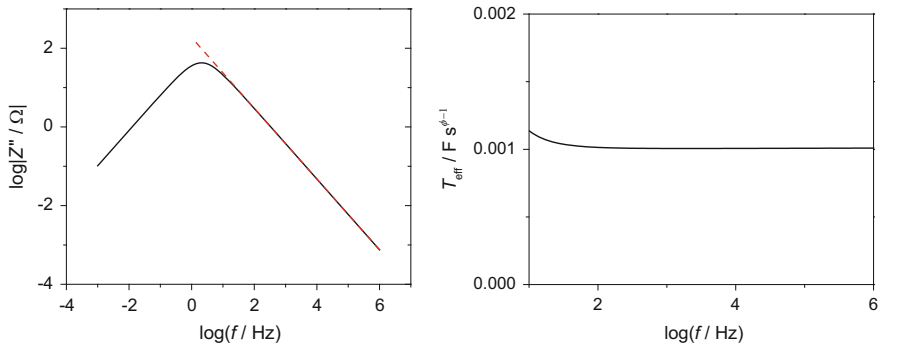

Fig. 8.5 Plots of $\log|Z''|$ versus $\log f$ and T_{eff} versus $\log f$ for $R_s(R_{ct}CPE)$ circuit with $R_s = 10\ \Omega$, $R_{ct} = 100\ \Omega$, $T = 0.001\ F\ s^{\phi-1}$, and $\phi = 0.9$

$$\omega_c = \left(\frac{1}{R_{ct}T}\right)^{1/\phi}, \tag{8.14}$$

which leads to

$$\overline{C}_{dl} = T^{1/\phi}\left(\frac{1}{R_{ct}}\right)^{1-\frac{1}{\phi}}, \tag{8.15}$$

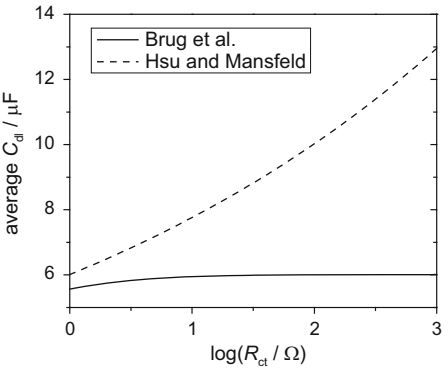

Fig. 8.6 Comparison of average values of interfacial capacitance, $\overline{C}_{dl}$, using Brug et al. [305] and Hsu and Mansfeld [306], Eqs. (8.15) and (8.16), as functions of charge transfer resistance, R_{ct}. Parameters: $R_s = 10\ \Omega$, $T_{dl} = 20\ \mu F\ s^{\phi-1}$, $\phi = 0.9$

and it can be compared with Brug et al.'s [305] formula:

$$\overline{C}_{dl} = T^{1/\phi}\left(\frac{1}{R_s} + \frac{1}{R_{ct}}\right)^{1-\frac{1}{\phi}}. \tag{8.16}$$

The difference between these two equations is related to the presence of an additional term $1/R_s$ in Brug et al.'s formula. In fact, they merge when $R_s \gg R_{ct}$. A comparison of the estimation of $\overline{C}_{dl}$ using Eqs. (8.15) and (8.16) is shown in Fig. 8.6. It is evident that the value obtained from the Hsu and Mansfeld model is very sensitive to the value of R_{ct}, and deviations between the $\overline{C}_{dl}$ values obtained increases with increases in R_{ct}. Several authors have indicated that Brug et al.'s formula seems to work better [307–311]. It should also be mentioned that it is often experimentally observed that when the parameter ϕ decreases, the value of T increases [213, 312, 313]. In such cases, Brug et al.'s formula produces smoother $\overline{C}_{dl}$ data because they are proportional to $T^{1/\phi}$.

8.2 Fractal Model

Real polycrystalline solid surfaces contain surface defects, scratches, irregularities, and pores, and their detailed geometry is usually unknown and cannot be exactly described. To describe such cases, a fractal model was proposed [314]. Fractal models describe self-similar surfaces in which further magnification reveals a self-similarity in which further magnification always shows a similar structure. Such a description could also be used to model random surface inhomogeneities. To better understand fractal scaling, let us look at a comparison of the fractal and classical magnifications shown in Fig. 8.7 [315]. Using a simple three times magnification (a → b), each element of the length l is increased three times in length, to 3 l. However, fractal magnification of each element (a → c) shows that it consists of additional similar elements. In the case presented in Fig. 8.7, each element l is

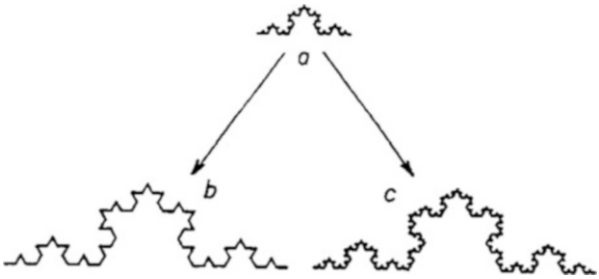

Fig. 8.7 Comparison of classical (**a**) and fractal (**b**) magnification; fractal dimension $D_H = 1.2619$ (From Ref. [315], copyright (1990), with permission from Elsevier)

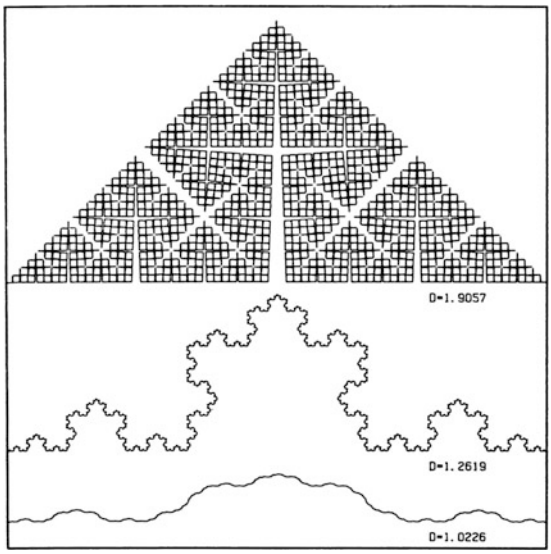

Fig. 8.8 Examples of von Koch curves for three different fractal dimensions (From ref. [317], copyright (1985), with permission from Elsevier)

increased four times in length, to 4 l. This leads to the fractal Hausdorf dimension [316], $D_H = \ln 4/\ln 3 = 1.2619$ [315, 317]. This dimension is larger than that of a simple magnification, which corresponds to a linear dimension of 1. This means that this simple fractal line has a dimension of 1.2619. A line consisting of self-similar segments scaled fractally is called a von Koch line [318]. This line has an infinite length as each magnification increases its length and is nowhere differentiable. A fractal structure is a mathematical model, but in nature, magnification is limited by the atomic structure and is limited to dimensions between 10 nm and 0.1 mm [315]. Examples of von Koch curves for three different fractal dimensions are shown in Fig. 8.8. The fractal dimension of a line may be between $1 \leq D_h < 2$ and for the surfaces $2 \leq D_h < 3$. As the fractal dimensions increase, the complexity of the line increases.

The concept of fractals was introduced for electrochemical impedance by Le Méhauté and coworkers [319, 320] and later developed by Nyikos and Pajkossy [317, 321–328]. They showed that the fractal geometry of a blocking interface leads to constant phase element behavior, Eq. (8.6).

Fractal theory was subsequently extended to irregular or quasi-random surfaces lacking well-defined self-similarity [323, 326, 329–331]. Pajkossy and Nyikos [332] carried out simulations of blocking electrodes with a self-similar spatial capacitance distribution and found that the calculated impedances exhibited CPE behavior.

It was found subsequently that, although fractal geometry produces CPE behavior, in practice there is no relation between the CPE exponent and fractal dimensions [333, 334]. Qualitatively, however, higher fractal dimensions lead to smaller values of ϕ. This is related to the different type of fractals like Cantor bars [335–338] or Sierpiński carpets [339–341], for which different relations hold. This means that the impedance technique does not allow for the determination of the surface fractal dimension. Such information can be obtained by the analysis of current-time curves in the presence of diffusion to the surface [323, 324, 342–344].

Fractal theory has also been applied to systems with faradaic reactions [315, 323, 324, 345, 346]. De Levie [315, 345] showed that the impedance of a fractal electrode in the presence of a simple faradaic reaction but in the absence of dc current is

$$\hat{Z} = R_s + \frac{1}{b}\left(\frac{1}{\frac{1}{R_{ct}} + j\omega C_{dl}}\right)^{\phi}, \tag{8.17}$$

where the parameter b is [317, 345]

$$b = f_g \rho_s{}^{\phi-1}, \tag{8.18}$$

ρ_s is the solution resistivity, and f_g is a geometric factor depending on the fractal surface geometry. De Levie [345] specified that this factor reflects the fact that a fractal description ignores details of the surface morphology, focusing only on the global response, and different surface geometries can have the same fractal dimension but different geometric factors f_g. Of course, for flat surfaces $\phi = 1, f_g = 1$, $b = 1$. Equation (8.17) is formally identical with that postulated by Davidson and Cole [298] for dielectric studies.

Although the CPE and fractal systems give the same impedance in the absence of redox reactions, a comparison of Eq. (8.9) for the CPE model with Eq. (8.17) for a fractal system in the presence of a redox reaction shows that they are structurally different. In fact, they produce different complex plane and Bode plots. This is clearly visible from Fig. (8.9), which can be compared with Fig. 8.4 for the CPE model. With a decrease in the value of ϕ, an asymmetry on the complex plane plot occurs that is also visible on the phase angle Bode plots. This is related to the different topology of the equivalent circuits; they are compared in Fig. 8.10. In the CPE model, only the impedance of the double-layer capacitance is taken to the power ϕ, while in the fractal model the whole electrode impedance is taken to the power ϕ. The asymmetry of the complex plane and Bode plots for fractal systems arises from the asymmetric distribution function of time constants in Eq. (8.4) according to the equation [298, 347]

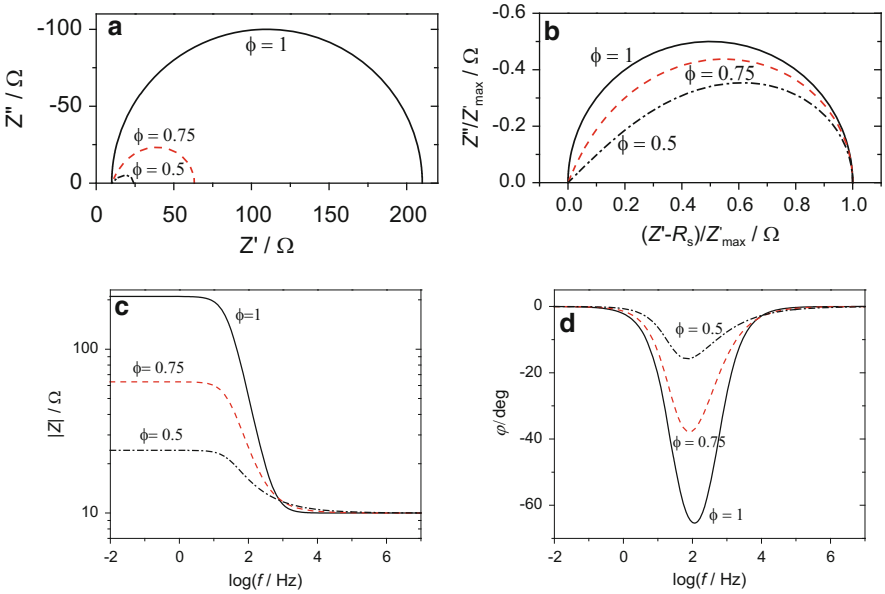

Fig. 8.9 Complex plane (**a**), normalized complex plane (**b**), and Bode plots (**c**, **d**) for fractal model with redox reaction, Eq. (8.17), assuming the following parameters: $R_s = 10\ \Omega$, $R_{ct} = 200\ \Omega$, $C_{dl} = 20\ \mu F$, $b = 1$, and various values of ϕ

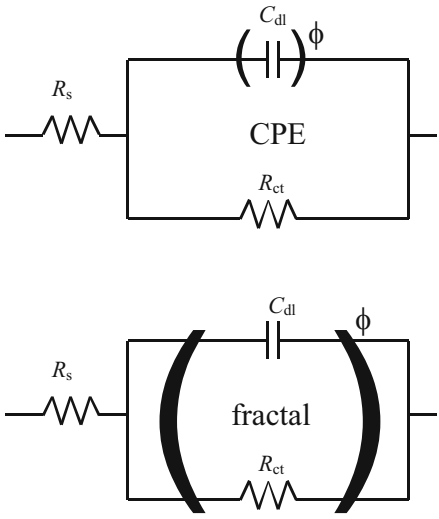

Fig. 8.10 Comparison of CPE and fractal models for systems with faradaic reaction

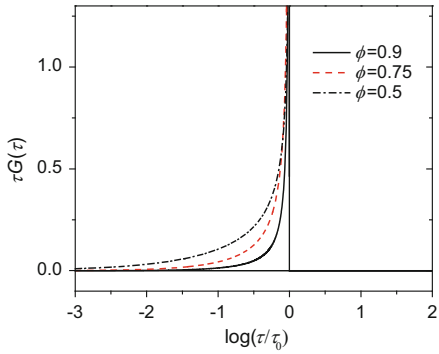

Fig. 8.11 Time constant distribution function for fractal model for different values of ϕ

$$\tau G(\tau) = \begin{cases} \dfrac{\sin(\phi\pi)}{\pi} \left(\dfrac{\tau}{\tau_0 - \tau} \right)^{\phi} & \text{for } \tau < \tau_0, \\ 0 & \text{for } \tau > \tau_0, \end{cases} \tag{8.19}$$

which means that the time constants are dispersed only up to the maximal value τ_0. The plot of this function is shown in Fig. 8.11. It is evident that the distribution function is asymmetric.

Because of the presence of the unknown parameter f_g in Eq. (8.18), it impossible to determine the value of the factor b, and the values of the charge transfer resistance and double-layer capacitance remain unknown. From the experiment it is possible to determine only these parameters multiplied or divided by the factor $b^{1/\phi}$:

$$C_{\mathrm{dl,exp}} = C_{\mathrm{dl}} b^{1/\phi} \text{ and } R_{\mathrm{ct,exp}} = \frac{R_{\mathrm{ct}}}{b^{1/\phi}}. \tag{8.20}$$

8.3 Origin of CPE Dispersion

The presence of the CPE in experimentally measured impedances generated a lot of discussion and confusion in the literature [334]. Of course, the fractal model described earlier also leads to CPE behavior for blocking electrodes; however, in the presence of faradaic reactions it leads to skewed semicircles instead of a decrease in the center of the semicircle below the real axis, without the further deformation typically observed in experimental conditions (CPE behavior).

In general, the appearance of CPE-like behavior can be attributed to two phenomena:

1. Dispersion of time constants, $\tau = R_s C_{\mathrm{dl}}$;
2. Dispersion due to surface adsorption/diffusion processes (the so-called kinetic dispersion effect).

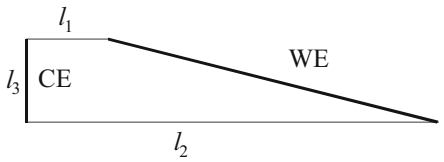

Fig. 8.12 Schematic representation of Hull cell used in simulations. *CE*, counter electrode, *WE*, working electrode

8.3.1 Dispersion of Time Constants

Schelder [348] attributed CPE dispersion to the microscopic surface roughness through bulk electrolyte conductivity; however, his branched *R-C* model does not seem to reflect correctly the actual current distribution [334]. Initially, CPE dispersion continued to be considered a consequence of surface microscopic roughness or porosity. However, surface porosity gives quite different effects (Chap. 9). Moreover, several authors [313, 334, 349, 350] demonstrated experimentally that an increase in the microroughness of a Pt electrode causes a decrease in the deviation from the ideal capacitive behavior, that is, the parameter ϕ becomes close to one for an electrochemically roughened surface. Even a very porous Pt powder microcavity electrode prepared by ball milling with a dispersing agent displays almost ideal low-frequency behavior with $\phi = 0.992$ [351]. In addition, for very porous gold-based electrodes, after the initial line at 45° a vertical line showing only a small deviation from the ideal behavior is observed on complex plane plots [352]. Simple estimation shows that the microscopic roughness of macroscopically flat electrodes could show the dispersion of the time constants in a very high (kHz to MHz) frequency range, contrary to the experimental observations of dispersion in a very wide frequency range [353].

In general, the distribution of the time constants $\tau = R_s C_{dl}$ can arise from

i. The distribution of solution resistances, R_s
ii. The distribution of double-layer capacitances, C_{dl}

The distribution of solution resistances is observed in the Hull cell [354] displayed in Fig. 8.12, where the distance between the working and the counter electrode changes between l_1 and l_2.

A simulation of impedances for different values of l_1 is shown in Fig. 8.13. When $l_1 < l_2$, dispersion of the impedances is observed displaying a CPE-like behavior but only in a limited frequency range. Adding a charge transfer resistance in parallel with the double-layer capacitance leads to a skewed semicircle with a radius lower than the assumed R_{ct}. When the two electrodes are parallel, no dispersion is observed and a correct result is obtained. Simulations of impedances in the presence of the redox reaction represented by R_{ct} is displayed in Fig. 8.14, where distorted semicircles are obtained.

It should be added that in the foregoing cases, the current lines are not parallel as the current is looking for a path of least resistance.

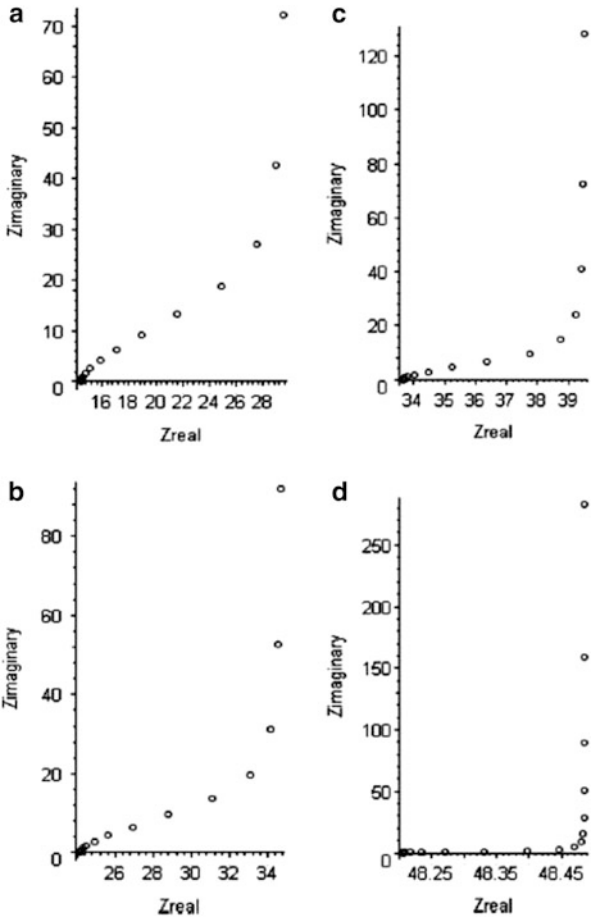

Fig. 8.13 Complex plane plots for ideally polarizable working electrode in Hull cells with different geometry; parameters: $\rho_s = 10\ \Omega$ cm, $C_{dl} = 20\ \mu F\ cm^{-2}$, $l_2 = 5$ cm, $l_3 = 1$ cm, $l_1 =$ (**a**) 1 cm, (**b**) 2 cm, (**c**) 3 cm, (**d**) 5 cm; see Fig. 8.12 for definitions of geometric parameters, (impedances are in Ω, imaginary part is negative) (From Ref. [354], copyright (2007), with permission from Elsevier)

Newman found that at disk electrodes current distribution is nonuniform in the radial direction (known as the primary [355] and secondary [356] current distributions), which leads to impedance dispersion [357]. Recently, Huang et al. [310, 358, 359] continued these studies in more detail using a local impedance approach. Global admittance corresponds to the integration of the local admittances over the total disk area. Impedance can also be defined (and experimentally measured) locally as a function of the position on the electrode surface. In the case of the disk geometry, it changes radially from the disk center, $r = 0$, to the disk radius, $r = r_0$. The authors distinguished two types of distribution of time constants:

a. 2D distribution arising from surface heterogeneities and geometry-induced nonuniform current and potential distribution.
b. 3D distribution arising from variations in properties normal to the electrode surface, for example, changes in the conductivity of oxide layers with the distance from the electrode surface.

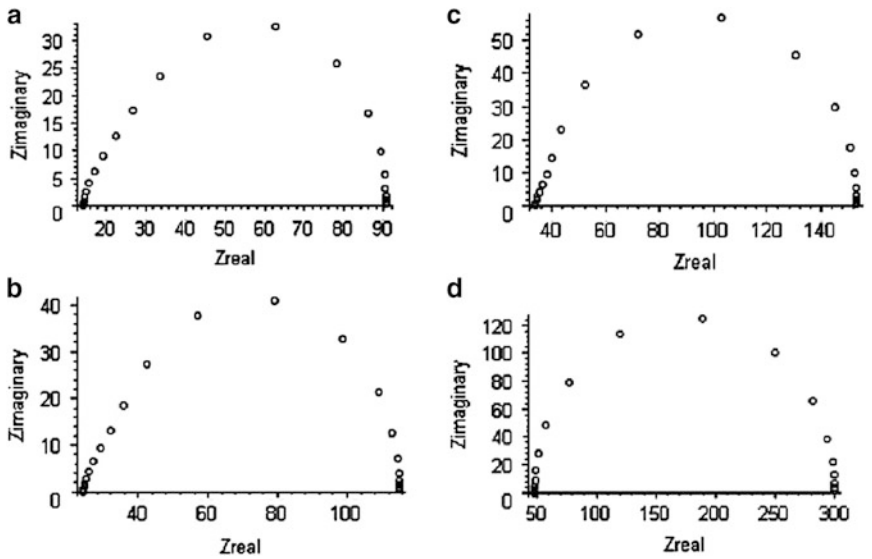

Fig. 8.14 Complex plane plots for faradaic reaction with $R_{ct} = 250\ \Omega\ cm^2$ in various Hull cells; cell parameters as in Fig. 8.13, (impedances are in Ω, imaginary part is negative) (From Ref. [354], copyright (2007), with permission from Elsevier)

The local impedance, $z(r)$, consists of two contributions: the local interfacial impedance, $z_0(r)$, and the local ohmic solution impedance, $z_e(r)$:

$$z(r) = z_0(r) + z_e(r), \tag{8.21}$$

and the global impedance, Z, is obtained by integration of the admittances:

$$Z = \left(2\pi \int_0^{r_0} \frac{1}{z(r)} r \ \mathrm{d}r \right)^{-1}, \tag{8.22}$$

where $z_0(r)$ is measured between the electrode surface and a point just outside the diffuse double layer, and $z_e\,(r)$ is measured in solution between the point outside the diffuse layer and the reference electrode at infinity. The behavior of the total electrode impedance for an ideally polarizable electrode obtained at a disk electrode is shown in Fig. 8.15. This behavior depends on the dimensionless frequency factor, K, defined as

$$K = \frac{\omega C_{dl} r_0}{\kappa}, \tag{8.23}$$

where C_{dl} is the specific double-layer capacitance and κ is the solution-specific conductivity. At frequencies corresponding to $K < 1$ the electrode behaves as an ideal capacitance, whereas for $K > 1$ deviations are observed (in accordance with

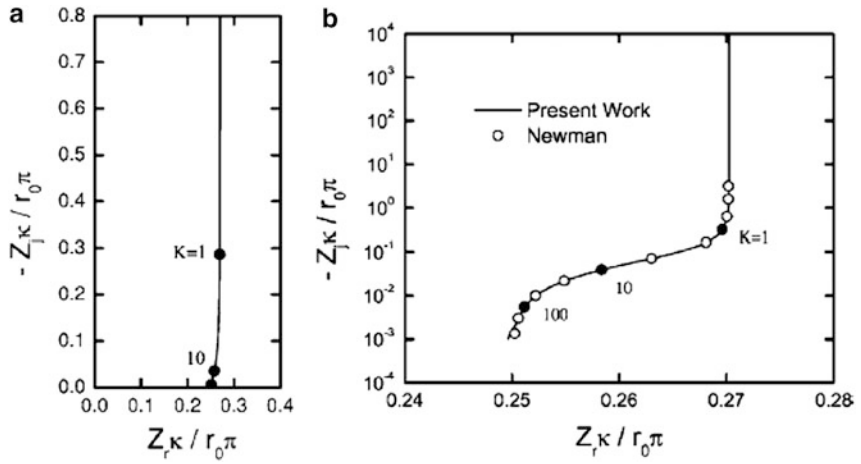

Fig. 8.15 Simulated complex plane plots of impedance response for ideally polarized disk electrode: (**a**) linear plot showing effect of dispersion at frequencies $K > 1$ as deviation from vertical line; (**b**) plot in logarithmic scale for imaginary impedances (From Ref. [358]. Reproduced with permission of Electrochemical Society)

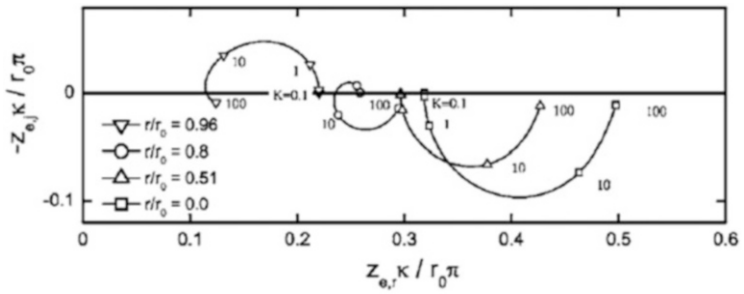

Fig. 8.16 Complex plane plots of normalized local ohmic impedance for different positions at disk surface, r/r_0 (From Ref. [358]. Reproduced with permission of Electrochemical Society)

Newman's predictions [357]). These deviations are more clearly visible on the logarithmic plot. It is interesting to note that the local interfacial impedance corresponds to an ideal capacitance, while the local ohmic impedance displays a more complicated behavior showing capacitive or inductive effects, see Ref. [359].

This means that the deviations from the ideal capacitive behavior observed for global impedance at high frequencies originate from the behavior of the local ohmic solution impedance (Fig. 8.16) caused by a nonlinear current and potential distribution at disk electrodes [360]. Similar effects were observed in the presence of faradaic reactions [310, 361, 362]. Theory discussed above was experimentally verified for corroding materials [359, 360, 363] or film thickness [311, 364, 365]. It is important to note that the Brug et al. formula, Eqs. (8.15) and (8.16), seems to work much better than that of Hsu and Florian, Eq. (8.15) [310]. Moreover, the recessed disk electrodes for which the current distribution is uniform do not show such impedance dispersion and behave ideally [366].

Another possible source of dispersion of time constants is the dispersion of capacitances arising from atomic-scale surface inhomogeneities such as grain boundaries, crystal faces on a polycrystalline electrode, or other variations in surface properties [313, 334, 350, 358]. However, experimental studies do not confirm this hypothesis. In fact, an increase in surface roughness, that is, of surface inhomogeneities, does not decrease the CPE parameter ϕ but increases it and such a surface becomes more similar to the ideal capacitance [313, 334, 350].

8.3.2 Dispersion Due to Surface Adsorption/Diffusion Processes

Dispersion due to surface adsorption/diffusion processes, or the so-called kinetic dispersion effect, is related to slow, i.e., kinetically limited, adsorption of ions or neutral molecules (often impurities) at the electrode surface. It has also been observed for surface reconstruction and changes in the adsorption layer where sharp deviations from ideal behavior and drop of the CPE exponent appeared. It has been found that in very clean solutions at monocrystalline electrodes the CPE parameter ϕ is very close to unity, e.g., at Au(111) in 0.1 M $HClO_4$ it is 0.997 [367], which indicates a practically ideal capacitive behavior. However, in the presence of specifically adsorbed anions, this value is always smaller. This behavior could be explained by assuming diffusion-kinetics-controlled ionic adsorption [367–375] and is described by the Frumkin and Melik-Gaykazyan model [376, 377]. The rate of an ionic adsorption reaction, v, is described by the following equation [367]:

$$v = \frac{\mathrm{d}\Gamma}{\mathrm{d}t} = v_{\mathrm{ad}} - v_{\mathrm{d}}, \tag{8.24}$$

where subscripts ad and d denote adsorption and desorption, respectively, and Γ is the surface excess of adsorbed ions. The current related to this reaction is

$$j = F\frac{\mathrm{d}\Gamma}{\mathrm{d}t} = \frac{\mathrm{d}q^{\mathrm{M}}}{\mathrm{d}t} = -\gamma F v, \tag{8.25}$$

where γ is the electrosorption valency that is the charge transferred between the electrode and the adsorbed ion in reaction: $A^- + \lambda e = A_{ads}^{-1+\lambda}$, and q^{M} is the excess charge density in a metal electrode. Applying the standard linearization procedure the reaction impedance is obtained:

$$\hat{Z}_{\mathrm{f}} = R_{\mathrm{ad}} + \frac{1}{j\omega C_{\mathrm{ad}}} + \hat{Z}_{\mathrm{W,ad}}, \tag{8.26}$$

where R_{ad} and C_{ad} are the adsorption capacitance and resistance, respectively, and $\hat{Z}_{\mathrm{W,ad}}$ is the mass transfer impedance. The electrical impedance model is displayed in Fig. 8.17 and its elements are defined as

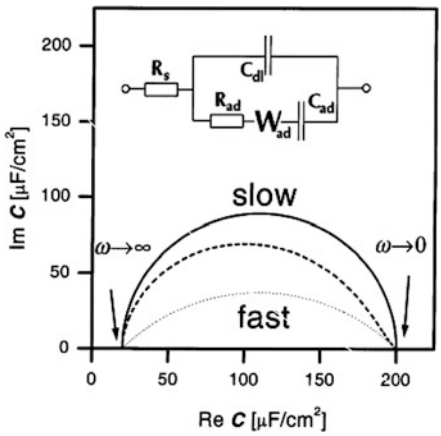

Fig. 8.17 Complex plane plots of complex capacitance, $\hat{C}$, defined using Eq. (8.28) for limiting cases of slow (*continuous line*), fast (diffusion limited, *dotted line*), and intermediate (*dashed line*) adsorption. Insert: equivalent electrical model for this process (From Ref. [367], copyright (2002), with permission from Elsevier)

$$C_{\mathrm{ad}} = \gamma F \frac{\left(\frac{\partial v}{\partial E}\right)}{\left(\frac{\partial v}{\partial \Gamma}\right)}; \quad R_{\mathrm{ad}} = -\frac{1}{\gamma F \left(\frac{\partial v}{\partial E}\right)};$$
$$\hat{Z}_{\mathrm{W,ad}} = \frac{\sigma_{\mathrm{ad}}}{\sqrt{j\omega}} = -\frac{1}{\gamma F \sqrt{j\omega D}} \frac{\left(\frac{\partial v}{\partial C}\right)}{\left(\frac{\partial v}{\partial E}\right)}, \tag{8.27}$$

where C is the bulk concentration of adsorbed ions, D their diffusion coefficient, and σ_{ad} the Warburg coefficient. Because complex plane plots are quite featureless, the analysis was carried out by transforming the impedances into complex capacitances:

$$\hat{C} = \frac{1}{j\omega\left(\hat{Z}_{\mathrm{tot}} - R_{\mathrm{s}}\right)} = C_{\mathrm{dl}} + \frac{1}{\frac{1}{C_{\mathrm{ad}}}\sigma_{\mathrm{ad}}\sqrt{j\omega} + R_{\mathrm{ad}}}. \tag{8.28}$$

Examples of complex capacitances simulated for kinetically slow, fast (i.e., diffusion limited), and intermediate adsorption rates are shown in Fig. 8.17. For the kinetically controlled reaction a perfect semicircle is observed and it becomes

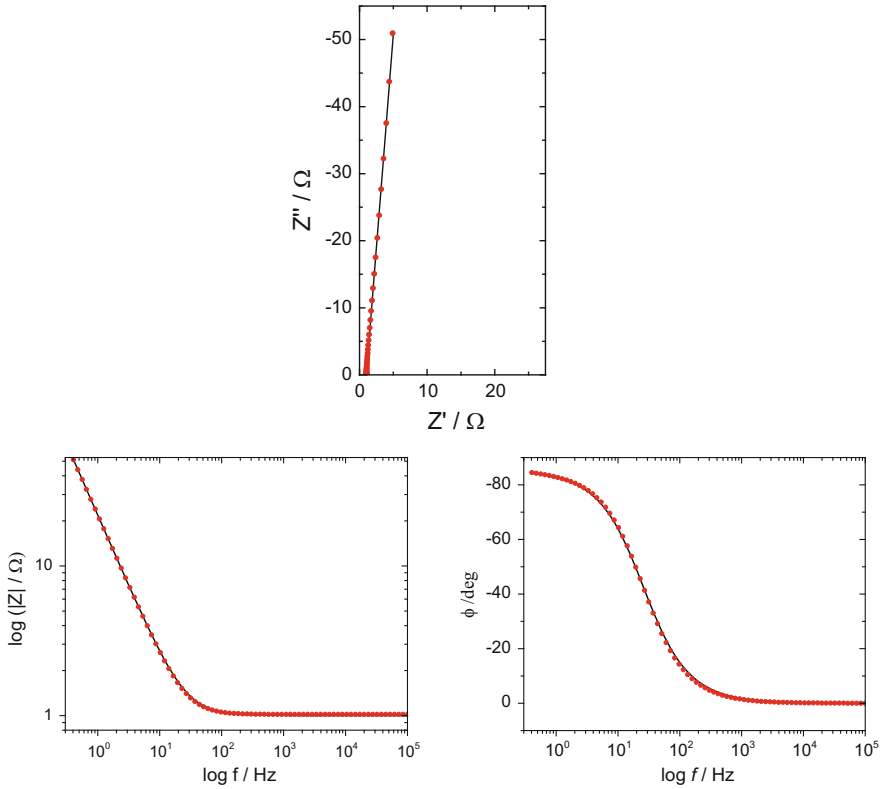

Fig. 8.18 Approximation of impedances simulated using CPE model with $T = 8$ mF $s^{-0.05}$, $\phi = 0.95$, and $R_s = 1\ \Omega$ (*points*) by kinetic Frumkin-Melik-Gayakazan model (*lines*)

distorted in the presence of mixed kinetic-diffusion control. Such an analysis was applied to study anionic adsorption on several well-defined metallic surfaces [367–375].

Experimental studies confirm that the CPE is often related to the adsorption of impurities. Studies performed on a polycrystalline Au electrode in the double-layer zone [352] in 1 M H_2SO_4 display almost ideal capacitive behavior with $\phi \sim 0.99$, while in the same cell on the same electrode in 1 M $NaNO_3$ a larger CPE deviation with $\phi \sim 0.93$ was observed because sodium nitrate is not as pure as sulfuric acid. Moreover, at well-polished and annealed polycrystalline Pt (roughness factor $R_f = 1.4$) the parameter ϕ is between 0.97 and 0.977 in the double-layer zone in 0.1 M H_2SO_4 [352]. However, after electrochemical roughening ($R_f = 5.1$) ϕ increases to >0.99. This can only be explained by the fact that the surface (ionic) impurities become distributed over a larger surface area and their coverage becomes smaller.

Although the CPE and the kinetic Frumkin and Melik-Gayakazan models are intrinsically different, they lead to the same impedance behavior in a certain frequency range.

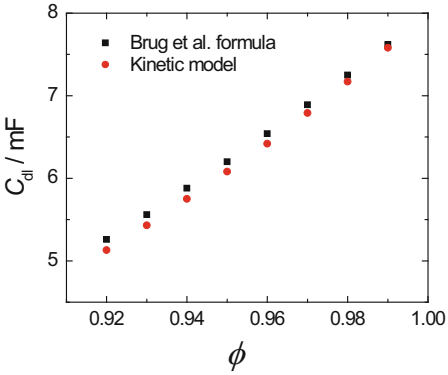

Fig. 8.19 Dependence of double-layer capacitance, $\overline{C}_{dl}$, determined using Brug et al. CPE model, Eq. (8.11), (▪), and C_{dl} estimated from kinetic model, (•), Eq. (8.26) (with $R_{ad} = 0$) determined from impedances simulated using CPE data: $T = 8$ mF $s^{\phi - 1}$, $R_s = 1$ Ω versus CPE exponent ϕ

Figure 8.18 shows complex plane plots simulated with the CPE model assuming $T_{dl} = 8$ mF $s^{-0.05}$ and $\phi = 0.95$. These data could be very well approximated [313] using the kinetic model with $C_{dl} = 6.08$ (0.02) mF, $\sigma = 0.0053$ (0.0001) Ω $s^{-1/2}$, $C_p = 2.83$ (0.01) mF, and $R_{ad} = 0$, where the numbers in parentheses denote the standard deviations of the parameters. The fit was carried out in the frequency range 100 kHz to 0.4 Hz and the goodness-of-fit parameter is $\chi^2 = 7.5 \times 10^{-4}$. At lower frequencies deviations appear. The obtained results indicate that both models might be indistinguishable in practice, although the CPE model contains fewer adjustable parameters.

If the experimental data arise from the kinetic model, the use of Brug's et al.'s formula cannot be justified. In fact, this formula leads, for the foregoing example, to an average value of $\overline{C}_{dl} = 7$ mF, while the true C_{dl} is 6.1 mF and $C_p = 2.8$ mF. Surprisingly, both values are relatively close to each other. However, the influence of the solution and charge transfer resistances in Brug et al.'s formula is relatively small because they are taken to the power $(1-\phi)/\phi$.

Data simulated using the CPE model and $T = 8$ mF $s^{\phi - 1}$, values of ϕ between 0.90 and 0.99, and $R_s = 1$ Ω could be approximated using the kinetic Frumkin-Melik-Gayakazan model, Eq. (8.26). Comparison of the values of C_{dl} from the kinetic model and $\overline{C}_{dl}$ obtained using Brug et al.'s formula, Eq. (8.11), is displayed in Fig. 8.19. The values obtained using the Brug et al.'s CPE model are close to those obtained using the kinetic model with a relative error from 2 % at $\phi = 0.9$ % to 0.5 % at $\phi = 0.99$. Similar approximations were obtained for lower values of the parameter T (corresponding to those obtained in the double-layer zone) but at frequencies higher than 4 Hz.

It should be stressed again that in the kinetic model the CPE-like behavior appears in a limited frequency range only.

8.4 Determination of Time Constant Distribution Function

As was shown earlier, the presence of the CPE of fractal impedance produces a distribution of the time constants. In addition, other elements such as the Warburg (semi-infinite or finite-length) linear or nonlinear diffusion, porous electrodes, and others also produce a dispersion of time constants. Knowledge about the nature of such dispersion is important in the characterization of electrode processes and electrode materials. Such information can be obtained even without fitting the experimental impedances to the corresponding models, which might be still unknown. Several methods allow for the determination of the distribution of time constants [378, 379], and they will be briefly presented below.

8.4.1 Regularization Methods

Equation (8.4), defining the time constant distribution function, is known as the Fredholm integral equation of the first kind:

$$g(\omega) = \int_0^\infty K(\tau, \omega) f(\tau) \mathrm{d}\tau, \tag{8.29}$$

where the left-hand side is a known function:

$$g(\omega) = \frac{\hat{Z}(\omega) - Z_\infty}{Z_0 - Z_\infty}, \tag{8.30}$$

$K(\omega, \tau)$ is a known kernel:

$$K(\omega, \tau) = \frac{1}{1 + j\omega\tau}, \tag{8.31}$$

and

$$f(\tau) = \tau G(\tau) \tag{8.32}$$

is the unknown time constant distribution function [248, 380–382]. Equation (8.29) can be solved numerically by its transformation into a system of linear equations:

$$\mathbf{g} = g(\omega) = \sum_{j=1}^{N} w_\mathrm{i} K_{\mathrm{i,j}} f_\mathrm{i} = \mathbf{KWg} = \mathbf{Af}, \tag{8.33}$$

where w_i are the coefficients corresponding to the quadrature used for integration, $K_\mathrm{ij} = K(\tau_i, \omega_j)$, $f_\mathrm{i} = f(\tau_\mathrm{i})$, and bold letters denote vectors or matrices. For example, for a simple trapezoidal integration rule the weights are $w_1 = w_\mathrm{N} = 0.5$ and the

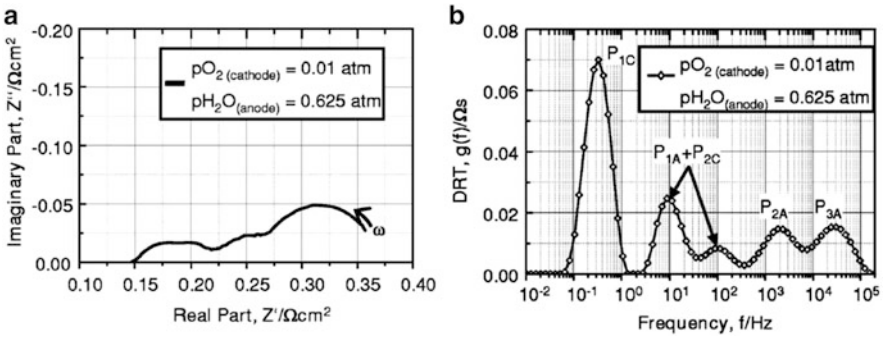

Fig. 8.20 Impedance spectrum and distribution of relaxation time function for solid oxide fuel cell (From Ref. [385]. Reproduced with permission of Electrochemical Society)

other $w_i = 1$. The linear system of equations $\mathbf{g} = \mathbf{Af}$ can be solved by minimizing the residuals using a least-squares method: minimize $\| \mathbf{Af} - \mathbf{g} \|^2$ with respect to $\mathbf{f}$. This leads to a known solution: $\mathbf{f} = (\mathbf{A}^T \mathbf{A})^{-1} \mathbf{A}^T \mathbf{g}$, where the index T denotes a transposed matrix. However, this procedure is an ill-posed problem involving the inversion of large matrices, and its solution leads to strong oscillations of $f(\tau)$ due to experimental errors of the measured impedance. To stabilize the solution, regularization techniques must be used depending on the value of the regularization parameter λ, which smooths function $\mathbf{f}$. The biggest problem is how to choose the optimal value of λ because too small values of λ allow oscillations and too large values distort the function (too much damping). There are, however, several methods of regularization and determination of the optimal values of the regularization parameter [383]. It was found using data simulated for the CPE or fractal models that correct distribution functions were obtained [381, 382]. However, the results were sensitive to experimental errors, and for a more complicated model involving a finite-length porous model the distribution function obtained contained some oscillations around the large peak [382]. When these oscillations were damped, the data recalculated from the distribution function differed from the assumed values. This indicated that the regularization method was not reliable for determining the time constant distribution function.

Ivers-Tiffé and coworkers proposed a modification of the solution of Eq. (8.4) using a Fourier transform [384]. They applied their method to determine the time constant distribution in solid electrolytes and batteries [384–387]. An example of the application of this technique to solid oxide fuel cells (SOFCs) is shown in Fig. 8.20. The complex plane plot shows several poorly separated semicircles, while the time constant distribution function displays five peaks; the authors assigned these time constants to different processes.

8.4.2 Least-Squares Deconvolution Methods

The kernel in Eq. (8.31) corresponds to one element of a Voigt circuit, and the time constant distribution function, Eq. (8.32), is continuous. However, the integral in Eq. (8.4) can be substituted by a sum of discrete functions [378, 379]:

$$\frac{\hat{Z}(\omega) - Z_\infty}{Z_0 - Z_\infty} = \int_0^\infty \frac{G(\tau)}{1 + j\omega\tau} \mathrm{d}\tau = \sum_{m=1}^{M} \frac{g_\mathrm{m}}{1 + j\omega\tau_\mathrm{m}}, \tag{8.34}$$

where the continuous function $G(\tau)$ was replaced by a sum of discrete values g_m. For a series of fixed time constants uniformly distributed on a logarithmic scale, τ_m, the values of g_m might be determined by a complex nonlinear least-squares method. This method was implemented in J. Ross Macdonald's program LEVM (distributed at no cost on the Internet) [388]. Macdonald and Tuncer [378, 379] applied this method to study the dispersion of dielectric permittivities.

A modification of this procedure was proposed in the literature [389] and applied to determine the time constant distribution function [379]. This method is based on the predistribution of time constants uniformly on the logarithmic scale, and to improve the quality of the analysis, a Monte Carlo technique was used to increase the number of analyzed time constants. Approximation was carried out using a constrained least-squares method and led to a continuous distribution function. This procedure converted the nonlinear problem to a linear one from which g_m versus τ_m were obtained and produced positive values of the distribution function. The procedure was also applied to the distribution of the dielectric constants [379, 389].

8.4.3 Differential Impedance Analysis

Stoynov and coworkers [28, 390–398] proposed another method for the determination of the distribution of parameters called differential impedance analysis (DIA). It is based on the application of a simple three parameter $R_1(R_2C)$ model [a so-called local operating model (LOM)] to the impedance spectra. At each frequency three parameters Z′, Z″, and ω are known but they are not sufficient to determine the parameters R_1, R_2, and C. Therefore, two more parameters are added: dZ′/d logω and dZ″/d logω. This LOM is swept across the experimental impedance data producing series of the parameters at each frequency. The impedance of the LOM is

$$\hat{Z}_\mathrm{LOM} = R_1 + \frac{R_2}{1 + \omega^2\tau^2} - j\frac{R_2}{1 + \omega^2\tau^2} = R_\mathrm{eff}(\omega) + j\omega L_\mathrm{eff}(\omega) \tag{8.35}$$

where the model containing two frequency dependent parameters, R_eff and L_eff was introduced. Time constant may be found as $\tau = R_2C = (\mathrm{d}L_\mathrm{eff}/\mathrm{d}\ \log\omega)/(\mathrm{d}R_\mathrm{eff}/\mathrm{d}\ \log\omega)$ and then all the parameters using Eq. (8.35). To avoid oscillations, the

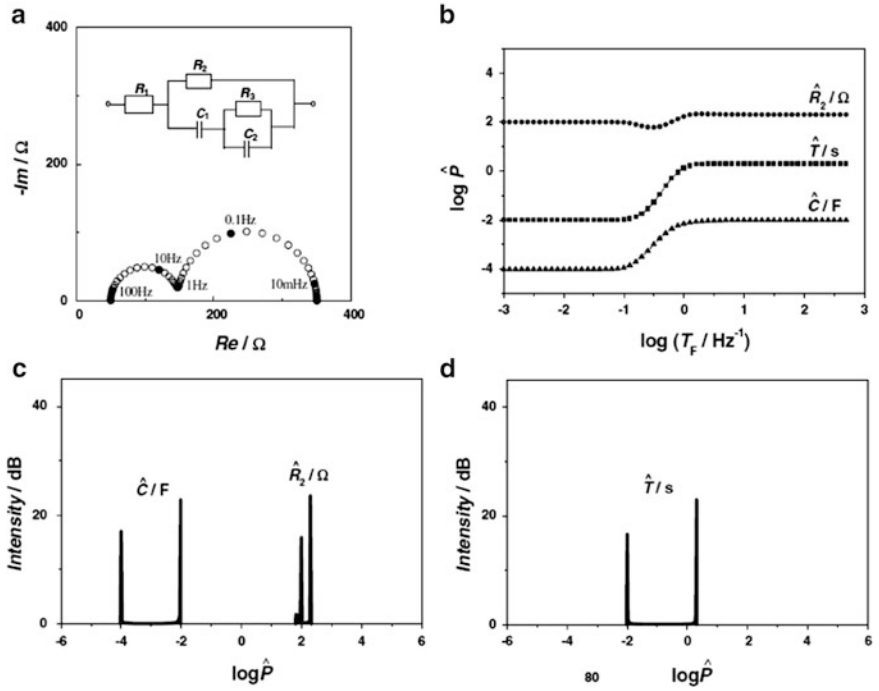

Fig. 8.21 Application of DIA to impedance data simulated using electrical equivalent model containing two time constants; (**a**) electrical equivalent model and impedance complex plane plot; (**b**) log of obtained parameters R_2, C, and time constant $\tau = T$ as functions of log of inverse frequency $\log T_F = -\log f_F$; (**c**) and (**d**) cumulative spectral line's intensity plots as functions of log of values of parameters (From Ref. [392], copyright (2004), with permission from Elsevier)

experimental data might be smoothed using splines. Let us look at the application of this method to the impedance data shown in Fig. 8.21a. Values of the parameters, $\hat{P}$, obtained as a function of the logarithm of frequency are displayed in Fig. 8.21b. It is obvious that there are two values of R_2, C, and the time constant $\tau = T$. Figure 8.21c, d shows the cumulative spectral line's intensity plots as functions of the logarithm of the parameter values. Now it is obvious that there are two time constants (d) and two values of the resistance and capacitance, in agreement with the model (a). To deal with the distributed elements as the CPE, the authors proposed a secondary DIA. The complex plane impedance plot for the CPE is shown in Fig. 8.22a, and the plot of the values of the parameters versus $\log T_f = -\log f$ are shown in panel b. There is a linear relation between the log of these parameters and $\log f$. Then one can determine the derivatives of these lines:

$$\delta_{P_i} = \frac{\mathrm{d}\ \log P_i}{\mathrm{d}\ \log \omega}, \tag{8.36}$$

which, according to the definition of the CPE, are $\delta_R = \alpha$, $\delta_C = 1 - \alpha$ and $\delta_T = 1$. These derivatives are shown in Fig. 8.22c as functions of $\log T_f$; they are constant,

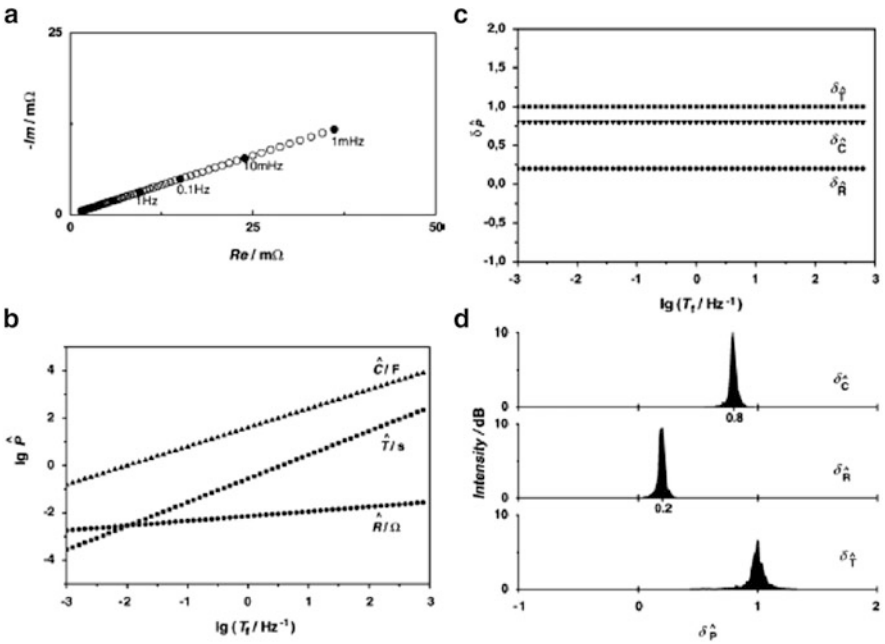

Fig. 8.22 DIA of CPE with $\phi = 0.8$ simulated in frequency range 10^3–10^{-3} Hz: (**a**) impedance diagram; (**b**) plot of CPE parameters versus $T_f = -\log f$; (**c**) differential temporal plots of parameters versus $\log T_f$; (**d**) differential spectral plots versus values of these derivatives (From Ref. [395], copyright (2006), with permission from Elsevier)

in agreement with the theory. Finally, the cumulative spectral line's intensity plots as functions of the logarithm of the parameter values are shown in panel d. The original value of the parameter ϕ is recovered. The DIA behavior of other distributed elements was shown in Ref. [28]. It should be added that DIA does not give directly the dispersion of the time constants but rather the dispersion of parameters that arises from the distribution of the time constants.

An example of the application of DIA to the impedance analysis of SOFCs is shown in Fig. 8.23.

8.4.4 Summary

Determination of the time constant distribution function is still carried out quite rarely. Several methods make it possible to determine this distribution function. Such procedures can be carried out without prior knowledge of the impedance model. Studies of the changes in the values and nature of time constants as functions of temperature or partial pressure of gases in SOFCs make it possible to assign these time constants to particular processes and to better understand the process mechanisms. The biggest drawback of this procedure is the lack of commercial programs allowing such an analysis. Mathematically, the simplest methods

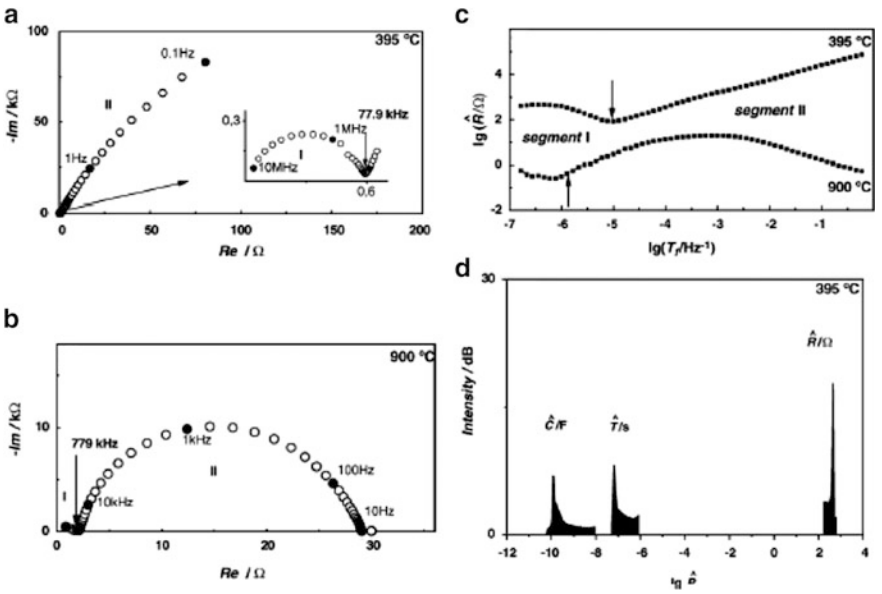

Fig. 8.23 Complex plane plots of YSZ single crystal in (**a**) 395 °C and (**b**) 900 °C; (**c**) plot of parameters versus $-\log f$; (**d**) spectral plot of determined parameters (From Ref. [395], copyright (2006), with permission from Elsevier)

are the least-squares deconvolution method (implemented in LEVM program) and the DIA, although some authors (Tuncer, program in Matlab [379]) intend to provide their programs.

8.5 Conclusion

The problem of impedance dispersion at solid electrodes is still a subject of heated discussion. The CPE model that is usually used in practice makes it possible to fit experimental data; however, from a physical point of view it cannot be valid in the whole frequency range. The main sources of dispersion are the distribution of solution resistances (e.g., Hull cells, disk geometry) and the adsorption of ionic impurities. It must be stressed that both processes contribute to dispersion in a limited frequency range; however, in many cases it is impossible to go to sufficiently low frequencies to notice this effect. Of course, it is difficult to carry out detailed studies of the origin of the observed CPE in each experimental case, and the CPE might be used in the modeling of experimental impedances. The use of the Brug et al. formulas (8.11) and (8.16) to estimate the average double-layer capacitance seems to be an acceptable compromise, although, fundamentally, they are not correct. However, in kinetic studies, it was noticed that the presence of the CPE did not affect the charge transfer resistances. In fact, studies of the kinetics of the HUPD at a polycrystalline Pt carried out in two different geometric arrangements produced quite different CPE ϕ exponents, but the determined charge transfer resistances were identical [399].